Available online at www.sciencedirect.com
ScienceDirect
European Journal of Mechanics B/Fluids 26 (2007) 632–649

Simulation of airflow fields and microparticle deposition in realistic human lung airway models. Part I: Airflow patterns

Zheng Li [a], Clement Kleinstreuer [b,*], Zhe Zhang [a]

[a] *Department of Mechanical and Aerospace Engineering, CFPD Lab, 3198 Broughton Hall, Campus Box 7910, North Carolina State University, Raleigh, NC 27695, USA*
[b] *Department of Mechanical and Aerospace Engineering and Department of Biomedical Engineering, CFPD Lab, 3198 Broughton Hall, Campus Box 7910, North Carolina State University, Raleigh, NC 27695, USA*

Received 26 January 2006; received in revised form 20 December 2006; accepted 13 February 2007

Available online 12 March 2007

Abstract

In Part I, transient and steady laminar airflow fields were simulated with an in-house finite volume code for realistic upper airway models subject to different inlet conditions and geometric features. Axial velocities and secondary flows were compared at key time levels during the acceleration/deceleration phase of inhaled air and for steady-state inhalation. The main results can be summarized as follows. Considering two acceleration and deceleration time levels during transient inhalation as well as steady-state inhalation generating the same inlet Reynolds number, $Re_{\text{in-mean}} = 1201$, the airflow patterns are quite similar. However, stronger axial and secondary velocities occur at all upper branch locations during flow deceleration because of the dynamic lingering effect. In general, the axial velocity profiles at steady state are very close to those at the point of deceleration. Variations in upper airway geometry, e.g., in-plane vs. out-of-plane configurations, have a significant effect on the airflow fields, although the primary airflow structures are similar in both idealized and more realistic airway configurations. The type of velocity inlet condition and existence of cartilaginous rings also influence the flow field; however, their impact is less important than changes in spatial angles.

Keywords: Asymmetric upper airways; Transient 3-D airflow simulations; Parabolic and realistic velocity inlet conditions; Local velocity distributions

1. Introduction

For health-effect reasons alone it is important to understand complex airflow fields and local deposition of toxic/therapeutic micro-particles in human lung airways. Weibel [1] provided idealized geometry data, i.e., a model of symmetrically bifurcating airways. In contrast, Horsfield et al. [2] published information on asymmetric airways obtained from a human lung resin cast. Modern imaging techniques allow for an even more detailed mapping of the human respiratory system. For example, Ley et al. [3] obtained from CT-scan data a semi-automatically generated trachea-bronchial tree and provided a simple example of airflow pattern. Tawhai [4] used a volume-filling algorithm

* Corresponding author. Tel.: +1 919 515 5261; fax: +1 919 515 7968.
E-mail address: ck@eos.ncsu.edu (C. Kleinstreuer).

0997-7546/$ – see front matter
doi:10.1016/j.euromechflu.2007.02.003

to generate lung airways from CT scans, while Cebral and Summer [5] employed CT scan results to construct a model of the tracheal and central bronchial airways and also computed the airflow pattern.

Detailed computer simulations of airflow patterns were either based on Weibel's Type A model [1] or some aspects of more realistic geometric data sources [2,6]. However, so far major features of actual upper lung airways with realistic inlet conditions have not been published. For example, Comer et al. [7] analyzed validated steady velocity and particle distributions in detail in symmetrical double bifurcation airway models. Zhang and Kleinstreuer and Zhang et al. [8–11] investigated transient flow pattern and particle transport in triple bifurcation models as well as micro/nanoparticle deposition in a symmetrically bifurcating human upper airway model. They provided basic physical insight to airflow structures and particle deposition patterns with their modeling results. Nowak et al. [12] computed the steady airflow and aerosol deposition in 23 generations in a symmetric model, and in 4 generations in the CT-based model. Based on the Weibel's Type B configuration, Liu et al. [13] constructed an asymmetric model of generations G4 to G6 and simulated steady flow fields for a Reynolds number range of 200–1600. The contributions so far were based on idealized Weibel configurations; thus, some realistic geometry effects were not considered. In contrast, Calay et al. [14] and Ertbruggen et al. [15] relied on modified versions of Horsfield's model [2] to simulate airflow fields and microparticle depositions. However, both research teams assumed steady flow, uniform inlet velocity conditions, sharp carinal ridges, and a smooth trachea.

Relevant *experimental* work has been typically done for single and double bifurcations. For example, Zhao and Lieber as well as Lieber and Zhao [16,17] measured steady and transient flow velocity distributions in a symmetric single bifurcation for different Reynolds numbers, while Tanaka et al. [18] measured the axial and secondary flow velocity distributions in a human central airway model.

In this paper, a more realistic asymmetric geometry model [2,6], with out-of-plane configurations was constructed to represent actual human upper airways. The following three problems have been addressed.

(i) Transient effects: matching steady-state Reynolds numbers, which capture transient effects, have been determined for symmetrical airway bifurcations [9]; hence, it is of interest to see if the same holds for asymmetrical airway configurations.

(ii) Influence of inlet conditions on airflow structures and ultimately particle deposition patterns in a realistic airway model.

(iii) Influence of geometric factors, e.g., spatial angles and tracheal rings, on airflow structures and particle deposition.

Instead of using a commercial software to investigate these problems, which typically lacks modeling flexibility and code portability, an in-house code "CFPD" (Computational Fluid-Particle Dynamics) was developed to simulate laminar airflow fields (Part I) as well as micro-particle transport and deposition (Part II) in human upper airways. It should be mentioned that exhalation is not considered in this paper because toxic or therapeutic aerosol uptake is more important [8,22] than clearance. Thus, mechanisms like "steady streaming" [20] or "trap and release" [21] are not addressed.

2. Theory

2.1. Airway geometry

Human lung airway structures are complex and quite variable; however, there are some common geometric characteristics. As mentioned, Horsfield et al. [2] took measurements of a resin cast of a representative human respiratory system from the trachea down to the respiratory bronchioles, focusing on its asymmetric property which is an important characteristic of the human lung. They used 'dichotomy' to generate the bronchial tree, which is divided into three zones, i.e., central bronchi, intralobar bronchi and bronchioles.

In the first two zones, the two daughter branches of the same parent branch have not only different diameters and lengths but also different spatial angles (the angle with respect to the direction of gravity), which in our model were obtained from Raabe et al. [6]. Thus, the present geometry model is representative of human lung airways (see Fig. 1(a) and Table 1). Fig. 2 depicts the extents of left and right generation segments as well as local cross-sectional Slices A–E.

To compare the geometric influence under steady state, two other models are used: (i) the in-plane model, i.e., the model without considering the spatial angle listed in Table 1; (ii) the out-of-plane model with tracheal ring. The

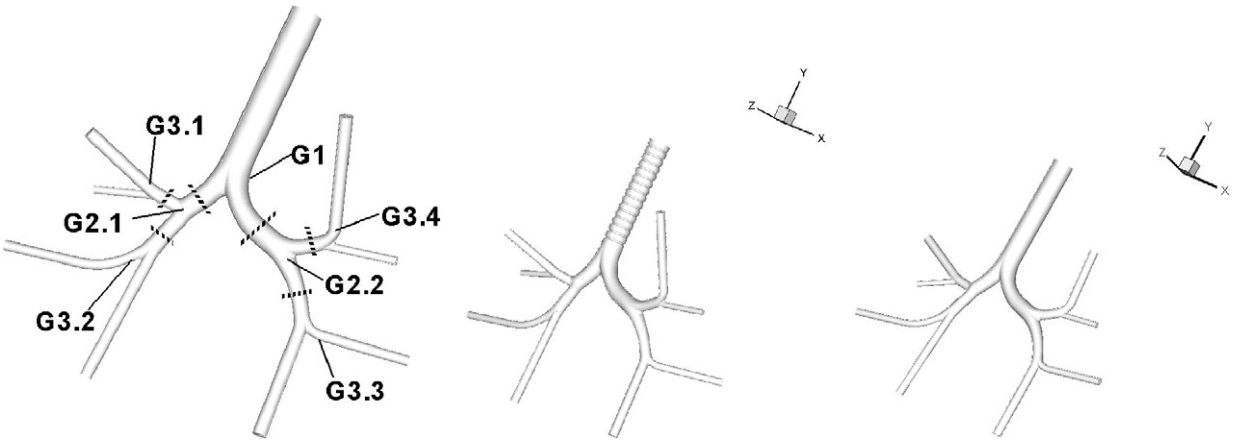

(a) (b) (c)

Fig. 1. Models of bronchial tree: (a) out-of-plane model without tracheal rings, (b) out-of-plane model with tracheal rings, (c) in-plane model without tracheal rings.

Table 1
Model geometry

Branch	Diameter (mm)	Length (mm)	In-plane branching half angle (degree)	Out-of-plane spatial angle (degree)
Trachea	16	100	0	0
L1	11.1	22.00	35	0
L2	7.3	15.60	63	25
L3	8.9	26.00	15	25
L4	6.67	11.27	18	60
L5	4.27	10.81	33	60
L6	5.2	21.00	61	5
L7	6.4	8.00	15	5
R1	12.0	50.00	73	0
R2	8.0	11.00	44	15
R3	7.5	16.00	48	15
R4	7.00	9.70	28	0
R5	5.35	9.70	70	0
R6	4.27	10.81	25	35
R7	6.67	11.27	65	35

dimensions of the tracheal rings were obtained from Zhang and Finlay [19]. There are 14 smooth rings of semicircular cross sections with a diameter of $0.1D_{\text{trachea}}$.

2.2. Governing equations

Assuming steady or transient laminar incompressible 3-D flow in rigid airways (see Fig. 1), the continuity and momentum equations are:

$$\frac{\partial u_i}{\partial x_i} = 0 \tag{1}$$

and

$$\frac{\partial u_i}{\partial t} + u_j \frac{\partial u_i}{\partial x_j} = -\frac{1}{\rho}\frac{\partial p}{\partial x_i} + \frac{\partial T_{ij}}{\partial x_j} \tag{2}$$

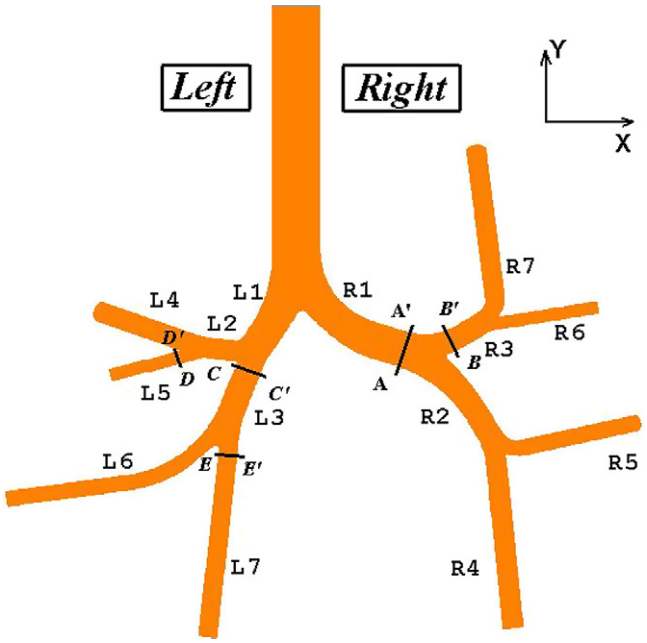

Fig. 2. Positions of local Slices A–E plus segmental extents L_i and R_i, $i = 1, \ldots, 7$.

where u_i is the local velocity, ρ is the density, p is the pressure, and T_{ij} is the stress tensor, i.e.,

$$T_{ij} = \upsilon\left(\frac{\partial u_i}{\partial x_j} + \frac{\partial u_j}{\partial x_i}\right) \tag{3}$$

where υ is the kinematic viscosity of air.

In this work, both steady and transient situations are simulated. For the steady-state cases, parabolic inlet velocity profiles as well as a realistic inlet airflow distribution after Zhang et al. [11] (see Fig. 3(a)(1)) were assumed. The realistic trachea-inlet velocity profile reflects the upstream effects of oral inhalation. For the transient simulations, the airflow rate at the inlet is time dependent. A realistic inhalation waveform under resting condition was employed [9] (see Fig. 3(a)(2)). In this case, the inlet velocity profiles were determined by the analytical expression of the transient fully developed flow in a straight tube, following the given input pulse expressed as Fourier series [9]. The "ghost-cells" method was employed to obtain the pressure values at the inlet, i.e., the pressure at the ghost cells is extrapolated from the inner cells. Extended outlet tubes assure fully-developed flow at all exits. At the outlets, the pressure boundary condition was used, i.e., the pressures at the outlets were set as constant.

2.3. Numerical method

The commercial software Solidworks (Solidworks Corporation, MA) was used to create the 3-D airway surfaces discussed in Section 2.1. The CAD-like data file was then transferred by Cadfix (International TechneGroup Incorporated, OH) into the mesh generator Gridpro (Program Development Company, NY). The finite-volume mesh was then read by the in-house code CFPD which outputs the airflow field.

The FORTRAN code CFPD is a cell-centered, finite volume multi-block solver. An upwind method was used to discretize the inviscid components of the Navier–Stokes equations, i.e., a Low Diffusion Flux Splitting Scheme (LDFSS) [23–25]. A second-order central difference scheme was used to discretize viscous and diffusive terms. The inviscid flux discretization is extended to second-order spatial accuracy using the slope-limited variable extrapolation technique.

For the transient flow simulation, an implicit scheme was formulated using the three-point backward time discretization in order to obtain second-order accuracy in time for the momentum equations. For the time integration, a dual-time Chorin's method was implemented [26]. When a dual time step is used, the artificial compressibility term

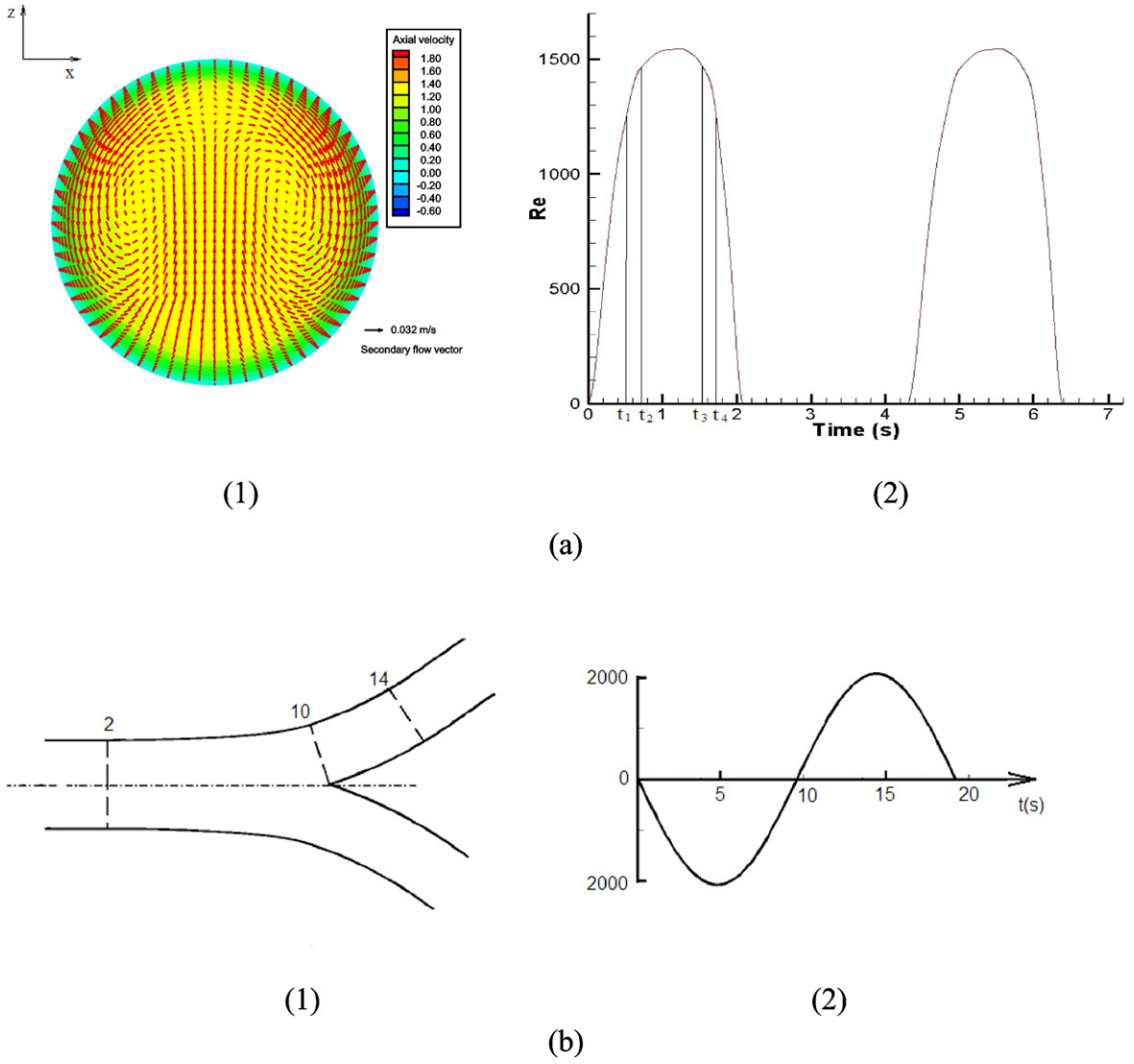

Fig. 3. Inlet conditions and schematics: (a) airflow inlet conditions: (1) realistic steady flow inlet condition (after Zhang and Kleinstreuer [8]) (Velocity is normalized as stated in Section 3.1.); (2) transient inlet wave form under resting condition; (b) schematic of single bifurcation [16,17]: (1) station positions; (2) input waveform.

is associated with the pseudo time only. Upon the convergence of this term in subiterations, the divergence free condition is restored as well as the incompressibility. During each subiteration, the solutions were updated by an implicit method, i.e., either planar Gauss–Seidel or block Incomplete LU (ILU) decomposition method.

In summary, fully implicit domain-decomposition parallel methods were implemented with the CPFD software. It allows all equations to be solved simultaneously, which is very advantageous for large-scale simulations.

The flow inlet/outlet conditions are adjustable where either the velocity or the pressure boundary condition can be implemented. FORTRAN and MPI libraries/compliers should be available on the computer platform. The number of processors used in the simulation depends on the capability of the processor cluster, the choices of CPU time and memory requirement. In general, best parallel computing efficiency depends on optimal balancing between the work-load over the number of processors (to reduce queuing time) and choosing block sizes with small surface-to-volume ratios (to reduce the amount of information that needs to be passed). The simulation results are stored in several files for each block. It is the user's responsibility to determine the format of the output files. The computations were performed on an IBM Blade Center Linux Cluster with multiple Intel Xeon 2.8 GHz processors. Generally, 24

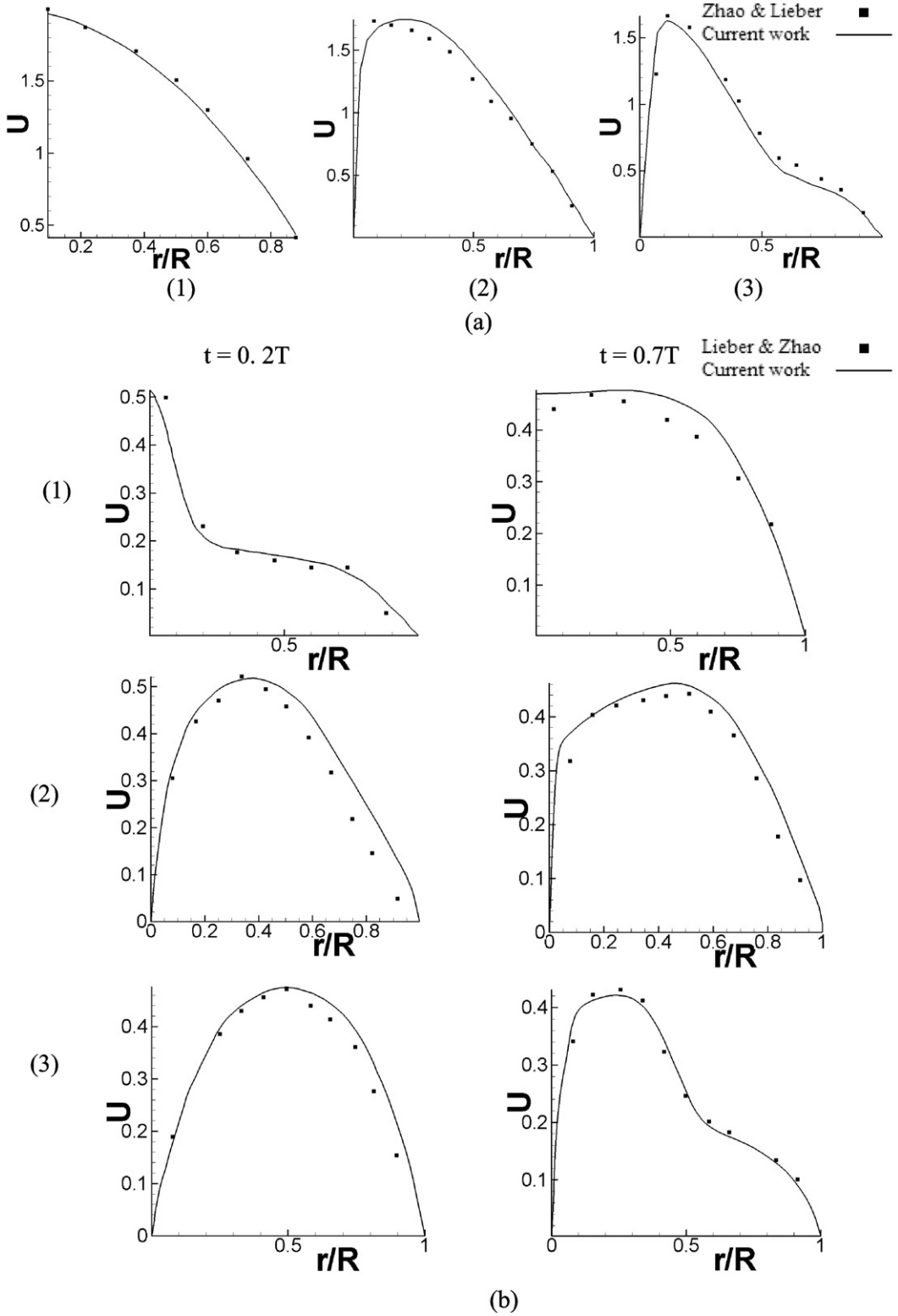

Fig. 4. Comparisons for axial velocity distribution: (a) steady state ($Re_{in} = 1036$, [16]): (1) station 2, (2) station 10, (3) station 14; (b) transient state ($Re_{in} = 1132$, [17]): (1) station 2, (2) station 10, (3) station 14.

processors were used. Typical run times for steady and cyclic flow simulations were approximately 2 and 200 hours (for 2.5 periods), respectively. Three different meshes, i.e., coarse, fine and very fine meshes, were employed to test grid independence of the results. Ultimately, the fine mesh was selected for the present study because it generated the same results as the very fine mesh.

2.4. Model validations

The current simulation code CFPD has been validated via comparisons with experimental data sets provided by Zhao and Lieber as well as Lieber and Zhao [16,17] (see Figs. 3(b) and 4). Both steady and oscillatory flows were considered. For details of these particular case studies, see Comer et al. [7] and Zhang and Kleinstreuer [8].

For steady flow, a fully-developed, i.e., parabolic, velocity profile can be observed in both numerical and experimental studies at location 2 (see Fig. 4(a)(1)). At location 10 (see Fig. 4(a)(2)), the velocity profile is skewed to the inner wall when the airflow turns from the parent to the daughter tube. When the airflow continuously turns, more fluid is pushed to the inner wall at location 14 (see Fig. 4(a)(3)) due to the effects of a centrifugal force and secondary flow. For the transient case, velocity profiles are significantly different at $t = 0.2T$ and $t = 0.7T$ due to the transient effect [8], where T is the period of inhalation. Generally, the average deviation between computational prediction and experimental data is less than 3%. During the inhalation period, which is emphasized in this work, the maximum average deviation is about 5.6% because of experimental uncertainties in fluid mass conservation. The good agreements indicate that the CFPD code is sufficiently accurate to simulate actual airflow in the human lung.

3. Results and discussions

3.1. Transient inhalation for out-of-plane airway model

In this section, transient inhalation is simulated considering the realistic out-of-plane configuration with a smooth trachea. A flow rate of $Q_{\text{in}} = 15$ l/min with period $T = 4.301$ s was selected, which represents typical human inhalation when resting (see Fig. 3(a)(2) and [9]). The simulations were performed for 2.5 periods in order to eliminate the initial flow field influence, where the representative Slices B–B′ to E–E′ (see Fig. 2) were selected for discussion. The Womersley number at the trachea ($Wo = a\sqrt{\omega/\upsilon}$, where a is the tube radius, ω is the angular frequency, and υ is the air kinematic viscosity) was 2.3 in this simulation. Generally, it is assumed that if Wo is greater than unity, the unsteadiness may become important; hence, transient effects are discussed in detail. Specifically, the simulation results (see Figs. 5–8) were recorded at $t_1 = 0.448$ s, $t_2 = 0.71$ s, $t_3 = 1.50$ s and $t_4 = 1.646$ s. At t_1 and t_4 the inlet Reynolds number was 1201 and at t_2 and t_3 $Re = 1468$, which are the mean Reynolds number and matching Reynolds number (see Part II), respectively. It should be noted that all velocities and speeds were normalized as $u/u_{\text{trachea-average}}$, where $u_{\text{trachea-average}}$ is the area-averaged mean velocity at the inlet of the trachea over one period.

Fig. 5 depicts the instantaneous axial and secondary flow fields at Slice B–B′ (see Fig. 2(a) for the slice location). Slice B–B′ is located in the right branch of generation G2.2. The symmetric, fully-developed velocity profile in the trachea becomes skewed where the maximum velocity is shifted to the inner wall after the flow turns the bend. When the air stream continues to turn from G1 to G2.2, the maximum velocity appears at the upper side (see Fig. 5(c)).

The flow patterns show similar shapes at different time levels as depicted in Fig. 5. However, for the axial velocity during acceleration, the flow is weaker when compared to the moment of deceleration for the same Reynolds number. Specifically, the axial velocity appears stronger at t_3 and t_4 when compared with t_1 and t_2(see Figs. 5(c)(1)–5(c)(4)). The steady-state velocity profile almost matches the instantaneous axial velocity when $t = t_4$ at $Re_{\text{in}} = 1201$ (see Fig. 5(a)). Considering secondary flow (see Fig. 5(b)), three large vortex regions are observed, with similar patterns at all four time levels. The maximum secondary velocities occur at the upper part close to the outer wall, which pushes air towards the outer wall.

A comparison of axial velocity along horizontal symmetric axis at Slice C–C′ in the transient state at t_1 and t_4 and for steady state using a Reynolds-number-equivalent profile is shown in Fig. 6(a). All velocity distributions exhibit highly nonlinear profile shapes. At $t = 1.646$ s, the flow velocity has the largest value. Figs. 6(b) and 6(c) show the secondary and axial flow patterns at Slice C–C′, respectively. As expected, quite different velocity profiles are observed at Slice C–C′ when compared to those at Slice B–B′ due to the different local Reynolds numbers and geometric characteristics. For the secondary flow, two relatively weak regions in the center area are observed during

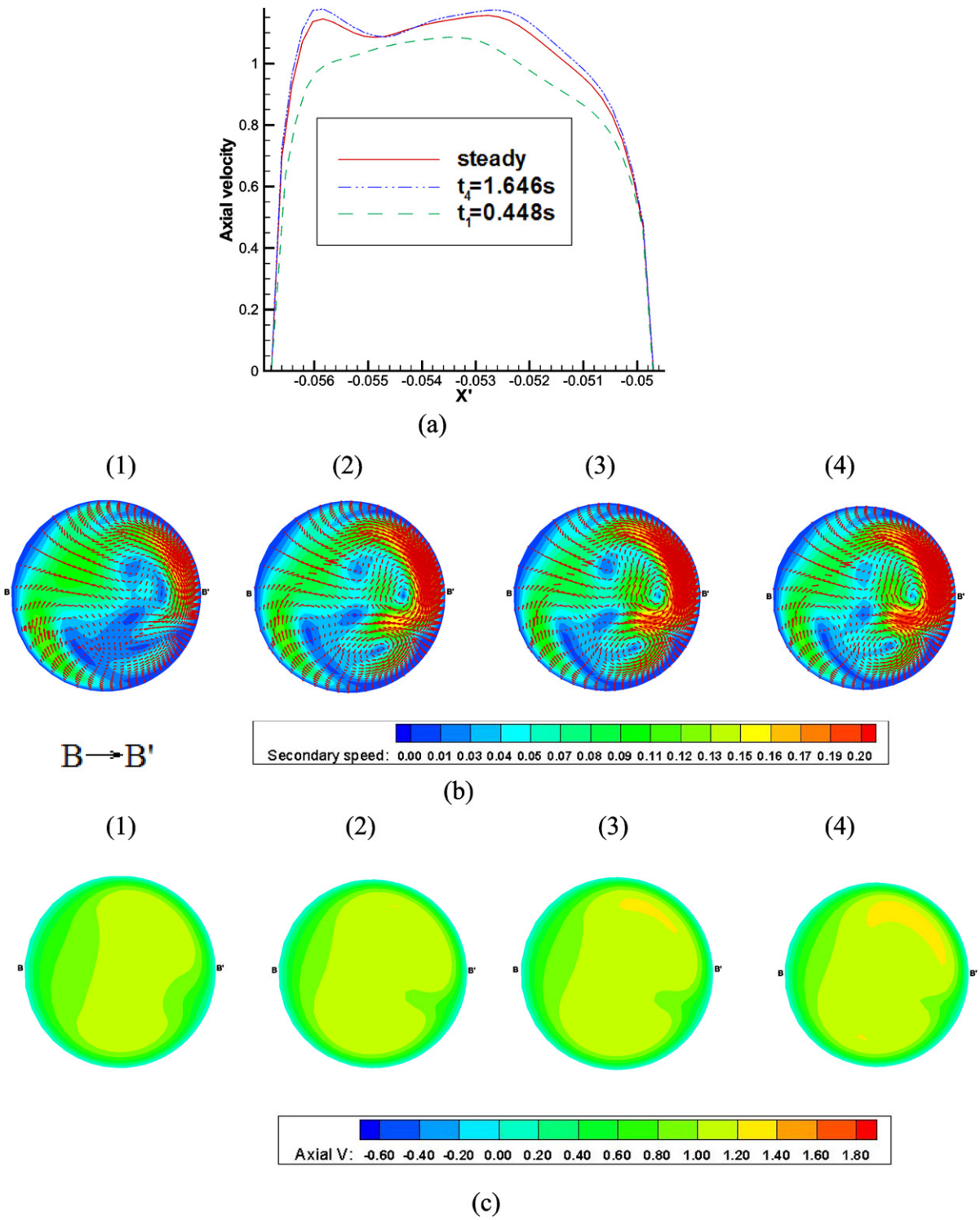

Fig. 5. Velocity distributions at Slice B–B′ (transient inhalation, out-of-plane G0–G3 model): (a) comparison of axial velocity profiles along horizontal symmetric axis; (b) secondary flow velocities: (1) $t_1 = 0.448$ s; (2) $t_2 = 0.71$ s; (3) $t_3 = 1.50$ s; (4) $t_4 = 1.646$ s; (c) axial velocities: (1) $t_1 = 0.448$ s; (2) $t_2 = 0.71$ s; (3) $t_3 = 1.50$ s; (4) $t_4 = 1.646$ s ($Re_{\text{in}} = 1201$ at t_1 and t_4, $Re_{\text{in}} = 1468$ at t_2 and t_3).

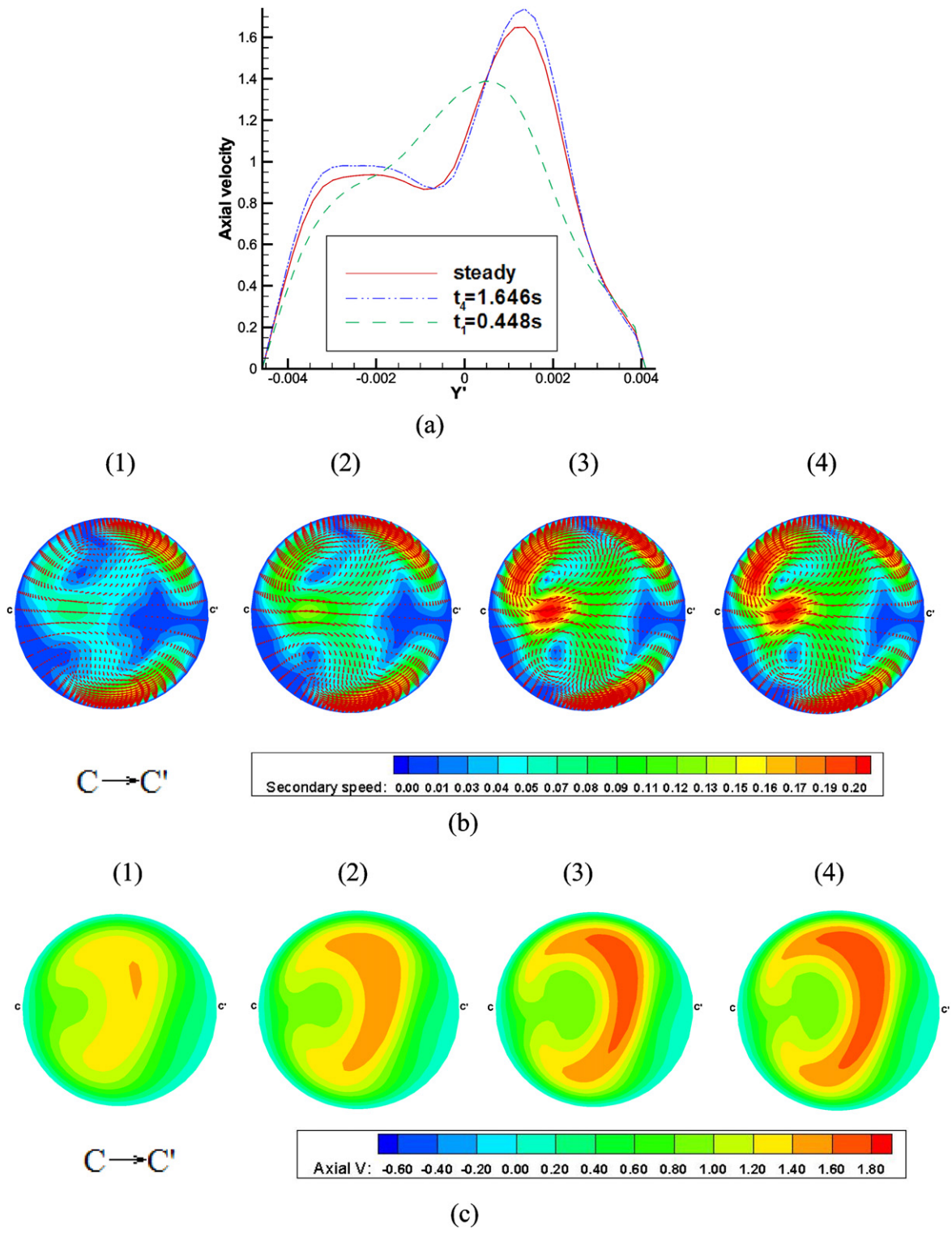

Fig. 6. Velocity distributions at Slice C–C′ (transient inhalation, out-of-plane G0–G3 model): (a) comparison of axial velocity profile along horizontal symmetric axis; (b) secondary flow velocities: (1) $t_1 = 0.448$ s; (2) $t_2 = 0.71$ s; (3) $t_3 = 1.50$ s; (4) $t_4 = 1.646$ s; (c) axial velocities: (1) $t_1 = 0.448$ s; (2) $t_2 = 0.71$ s; (3) $t_3 = 1.50$ s; (4) $t_4 = 1.646$ s ($Re_{\text{in}} = 1201$ at t_1 and t_4, $Re_{\text{in}} = 1468$ at t_2 and t_3).

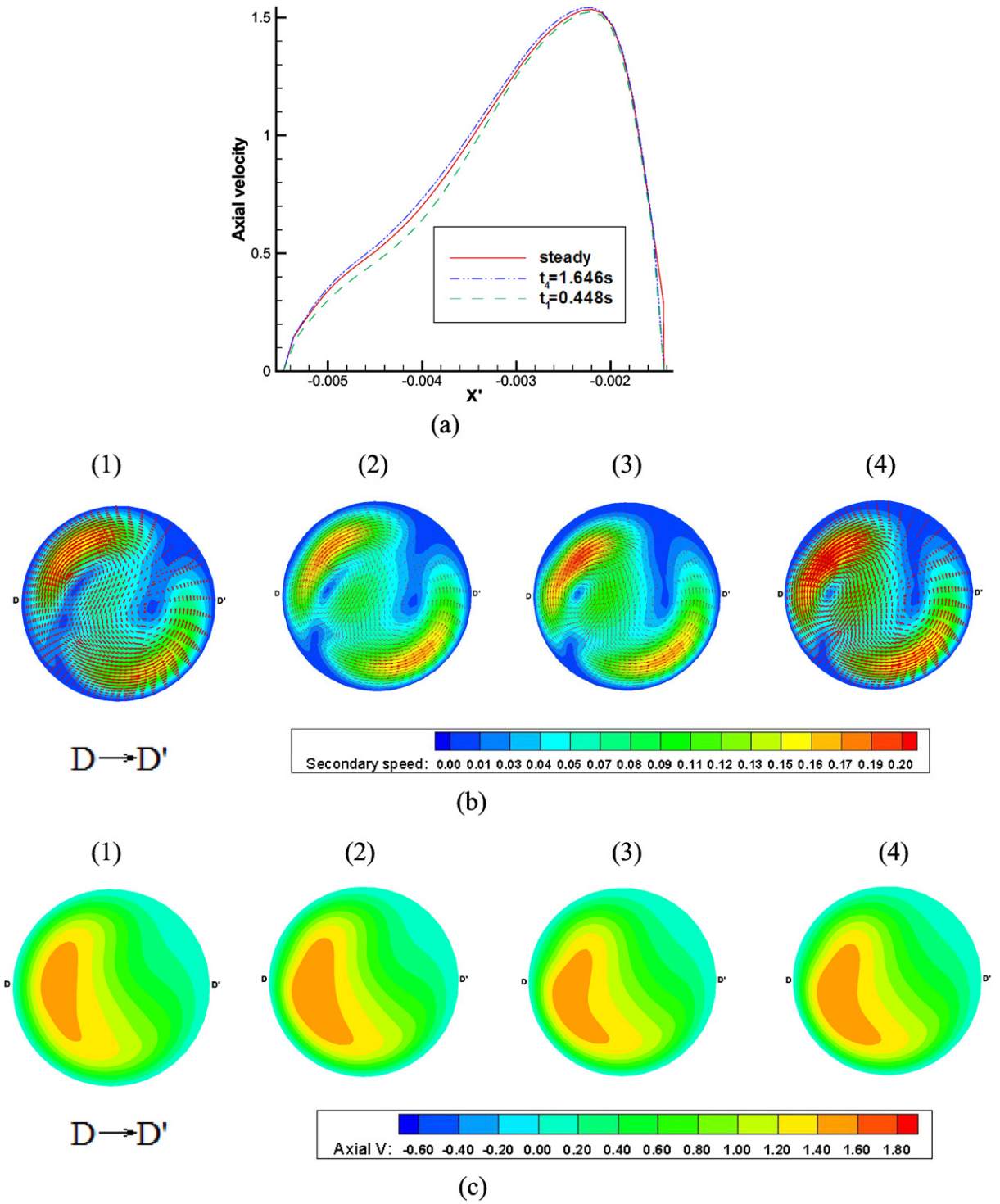

Fig. 7. Velocity distributions at Slice D–D′ (transient inhalation, out-of-plane G0–G3 model): (a) comparison of axial velocity profiles along horizontal symmetric axis; (b) secondary flow velocities: (1) $t_1 = 0.448$ s; (2) $t_2 = 0.71$ s; (3) $t_3 = 1.50$ s; (4) $t_4 = 1.646$ s; (c) axial velocities: (1) $t_1 = 0.448$ s; (2) $t_2 = 0.71$ s; (3) $t_3 = 1.50$ s; (4) $t_4 = 1.646$ s ($Re_{\text{in}} = 1201$ at t_1 and t_4, $Re_{\text{in}} = 1468$ at t_2 and t_3).

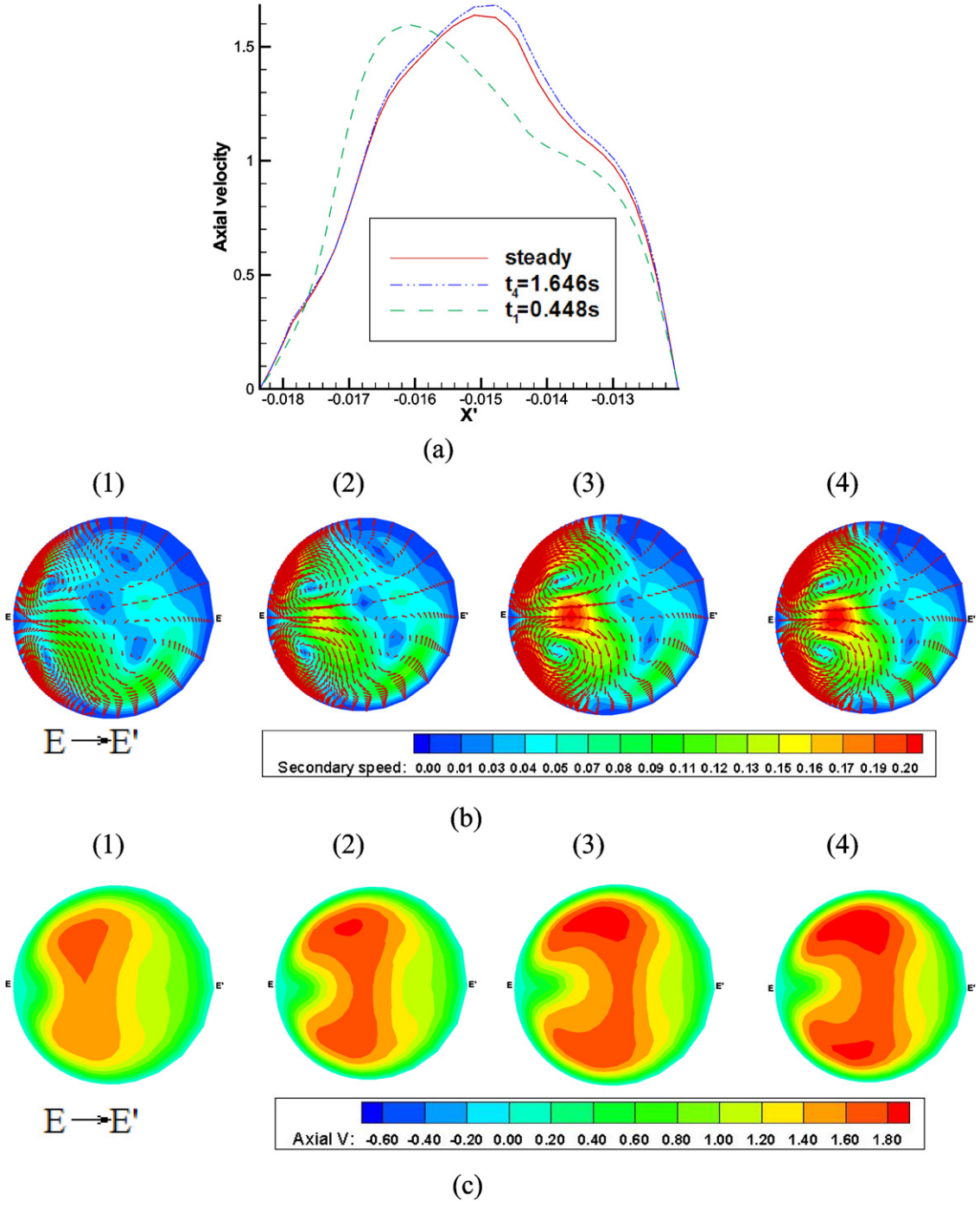

Fig. 8. Velocity distributions at Slice E–E′ (transient inhalation, out-of-plane G0–G3 model): (a) comparison of axial velocity profiles along horizontal symmetric axis; (b) secondary flow velocities: (1) $t_1 = 0.448$ s; (2) $t_2 = 0.71$ s; (3) $t_3 = 1.50$ s; (4) $t_4 = 1.646$ s; (c) axial velocities: (1) $t_1 = 0.448$ s; (2) $t_2 = 0.71$ s; (3) $t_3 = 1.50$ s; (4) $t_4 = 1.646$ s ($Re_{\text{in}} = 1201$ at t_1 and t_4, $Re_{\text{in}} = 1468$ at t_2 and t_3).

the acceleration, which become stronger during the deceleration phase, i.e., the secondary flow is stronger at t_3 and t_4 (Fig. 6(b)). The maximum axial velocity is close to the outer wall at all time steps due to the influence of the upstream flow. A higher velocity region appears at t_3 and t_4. Again, the flow patterns show somewhat similar shapes at different time levels especially in terms of secondary flows.

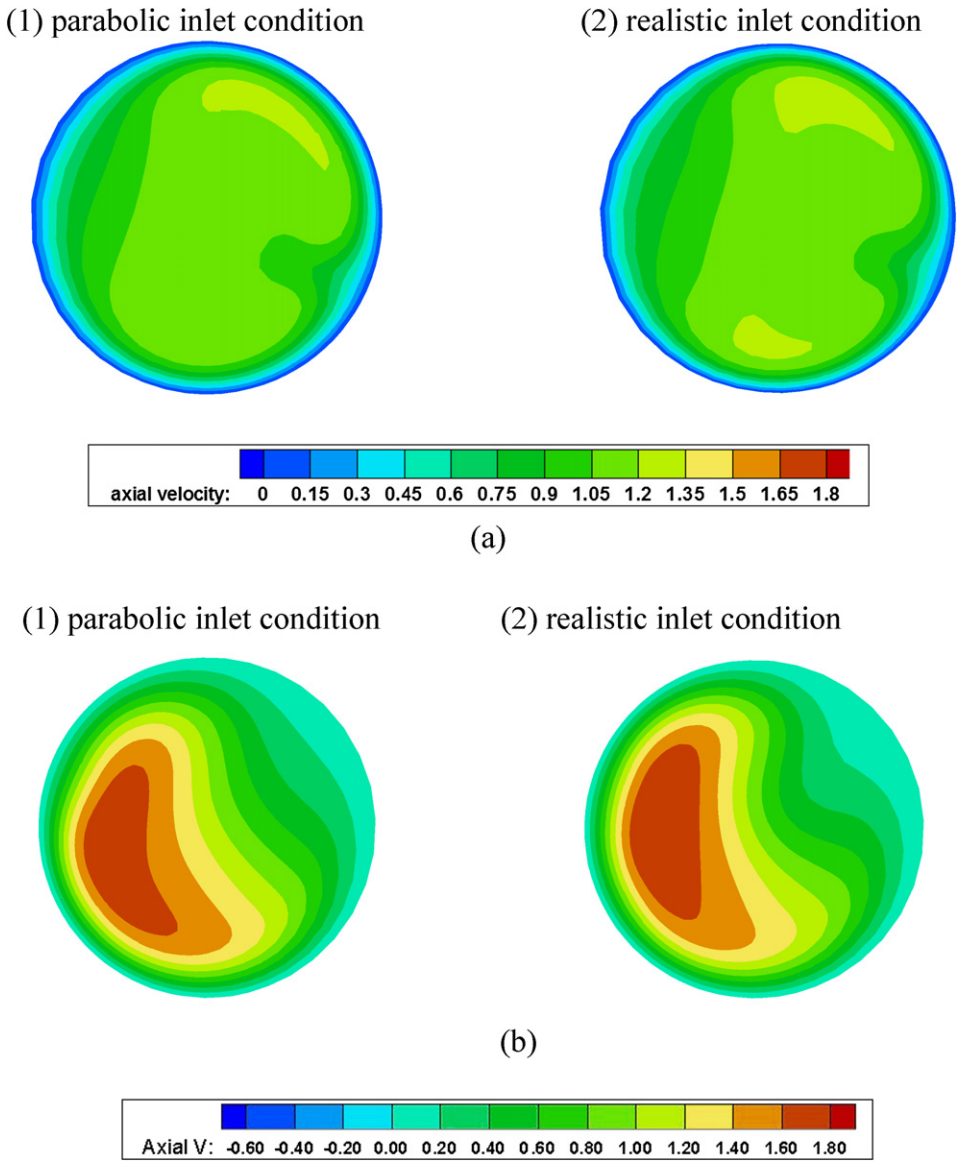

Fig. 9. Axial velocity distribution at Slice B–B′ and D–D′ ($Re_{in} = 1201$) : (a1) Slice B–B′, parabolic inlet condition; (a2) Slice B–B′, realistic inlet condition; (b1) Slice D–D′, parabolic inlet condition; (b2) Slice D–D′, realistic inlet condition.

The axial and secondary flow patterns at Slice D–D′ are shown in Figs. 7(a)–7(c). At this station, the changes occurring between different time levels are smaller, i.e., the three graphs are very close in Fig. 7(a). The most obvious difference appears for the secondary flow velocity distributions, where the higher velocity region varies stronger with time. But, they always appear at the same location which means that at this location the geometry influence dominates the flow distribution. In Figs. 7(c)(1)–7(c)(4), the flow patterns are still similar while the maximum axial velocity flow shifts around at the different time steps.

Fig. 8 depicts the axial and secondary flow patterns at Slice E–E′. Once again, the airflow fields are similar over time. Compared with Fig. 6, which shows the flow distribution in the parent branch, the maximum axial velocity shifts closer to the inner wall due to effects from secondary flow and local geometric features. The axial velocities along the horizontal symmetric axis at Slice E–E′ under different conditions are shown in Fig. 8(a). While retaining similar profile shapes, the maximum velocity shifts towards the inner wall at $t = t_1$. Focusing on secondary flows,

Table 2
Average and maximum velocity at t_1 and t_4 ($Re_{in} = 1201$)

			$t_1 = 0.448$ s	Steady	$t_4 = 1.646$ s
Slice B–B′	Average	Axial velocity	0.667	0.733	0.749
	value	Secondary flow velocity	0.046	0.061	0.067
	Maximum	Axial velocity	1.170	1.230	1.250
	value	Secondary flow velocity	0.168	0.229	0.256
Slice C–C′	Average	Axial velocity	0.642	0.780	0.823
	value	Secondary flow velocity	0.049	0.067	0.074
	Maximum	Axial velocity	1.410	1.703	1.792
	value	Secondary flow velocity	0.160	0.196	0.224
Slice D–D′	Average	Axial velocity	0.829	0.840	0.843
	value	Secondary flow velocity	0.058	0.063	0.066
	Maximum	Axial velocity	1.529	1.542	1.550
	value	Secondary flow velocity	0.162	0.178	0.188
Slice E–E′	Average	Axial velocity	0.604	0.709	0.741
	value	Secondary flow velocity	0.042	0.070	0.078
	Maximum	Axial velocity	1.664	1.900	1.981
	value	Secondary flow velocity	0.141	0.222	0.239

there are several vortices observed at all time levels. Still, the strength of the secondary flow is larger at t_3 and t_4, when compared to time levels t_1 and t_2.

In summary, the velocity profile shapes and flow patterns are somewhat similar during deceleration and acceleration for the same inlet Reynolds numbers. This also holds when comparing with the steady-state case, assuming a parabolic inlet profile. However, due to the dynamic "lingering effect", the flow velocity during the deceleration stage is generally larger than at the corresponding point of acceleration with the same Reynolds number and for steady flow. Furthermore, the velocity magnitude during the acceleration phase is usually less than for the corresponding steady-state case. Commonly, this effect is stronger in the lower-order branches, except when it is mitigated due to local changes in airway geometry. For example, at Slice D–D′, the influence of the lingering effect is less important because the complex geometry changes the flow patterns; i.e., although Slices D–D′ and E–E′ are both located in third-order branches, the influence of the lingering effect is different. Table 2 lists the average and maximum velocity at different slices for t_1 and t_4 ($Re_{in} = 1201$). It again shows that maximum values appear at t_4 rather than at t_1. Table 3 lists the velocity differences in axial and secondary flow velocities between time t_1 and t_4, as well as between t_1 and steady state for each case. It is observed that the secondary flow velocity changes are always larger than the axial velocity changes. It is also evident that the values at Slice E–E′ are generally much larger than at Slice D–D′. This is because the branching and spatial angles of the branch where Slice D–D′ is located are much larger than for Slice E–E′, which weakens the lingering effect.

3.2. Steady inhalation for out-of-plane airway model under different inlet conditions

As discussed in Section 3.1, the transient effect in the asymmetric bifurcation airway model is minor due to the relatively small Womersley number. More importantly, a matching steady-state Reynolds number has been found which matches transient inhalation, ultimately in terms of particle deposition fraction (see Part II). Hence, this section focuses on steady inhalation only, assuming both parabolic and realistic inlet velocity profiles. The results are compared at three representative locations: inlet plane, Slice B–B′ and Slice D–D′, which appear in the first, second and third order generation, respectively. The realistic inlet velocity profile was employed (see Fig. 3(a)(1)) because of the upstream effects. Though much weaker when compared to the axial velocity, the measurable secondary flow is introduced when using the realistic inlet condition.

Figs. 9(a)(1) and 9(a)(2) show the axial velocity distribution of the airflow at Slice B–B′. Evidently, the flow pattern becomes somewhat similar after the air has passed a certain distance from the trachea inlet to the lower region of G2.2. The most obvious difference appears in the lower part, where a higher velocity area is observed when the realistic inlet condition is applied. Figs. 9(b)(1) and 9(b)(2) depict the axial velocity distribution at Slice D–D′ in the third generation. Again, the asymmetric airflow structures are similar. High-velocity air is pushed to the left-upper and right-lower sides due to centrifugal forces and interaction with secondary flows. The high-velocity region shifts a

Table 3
Percentage changes in average and maximum velocities during acceleration when compared to steady flow and decelerating flow ($Re_{in} = 1201$)

			Steady (%)	t_4 (%)
Slice B–B′	Average value	Axial velocity	9.95	12.24
		Secondary flow velocity	32.95	47.63
	Maximum value	Axial velocity	5.12	6.81
		Secondary flow velocity	36.19	52.37
Slice C-C’	Average value	Axial velocity	21.41	28.08
		Secondary flow velocity	35.46	49.76
	Maximum value	Axial velocity	20.79	27.12
		Secondary flow velocity	22.15	39.99
Slice D–D′	Average value	Axial velocity	1.27	1.64
		Secondary flow velocity	9.47	15.13
	Maximum value	Axial velocity	0.88	1.37
		Secondary flow velocity	9.43	15.64
Slice E–E′	Average value	Axial velocity	17.22	22.66
		Secondary flow velocity	67.59	87.16
	Maximum value	Axial velocity	14.19	19.06
		Secondary flow velocity	56.97	68.74

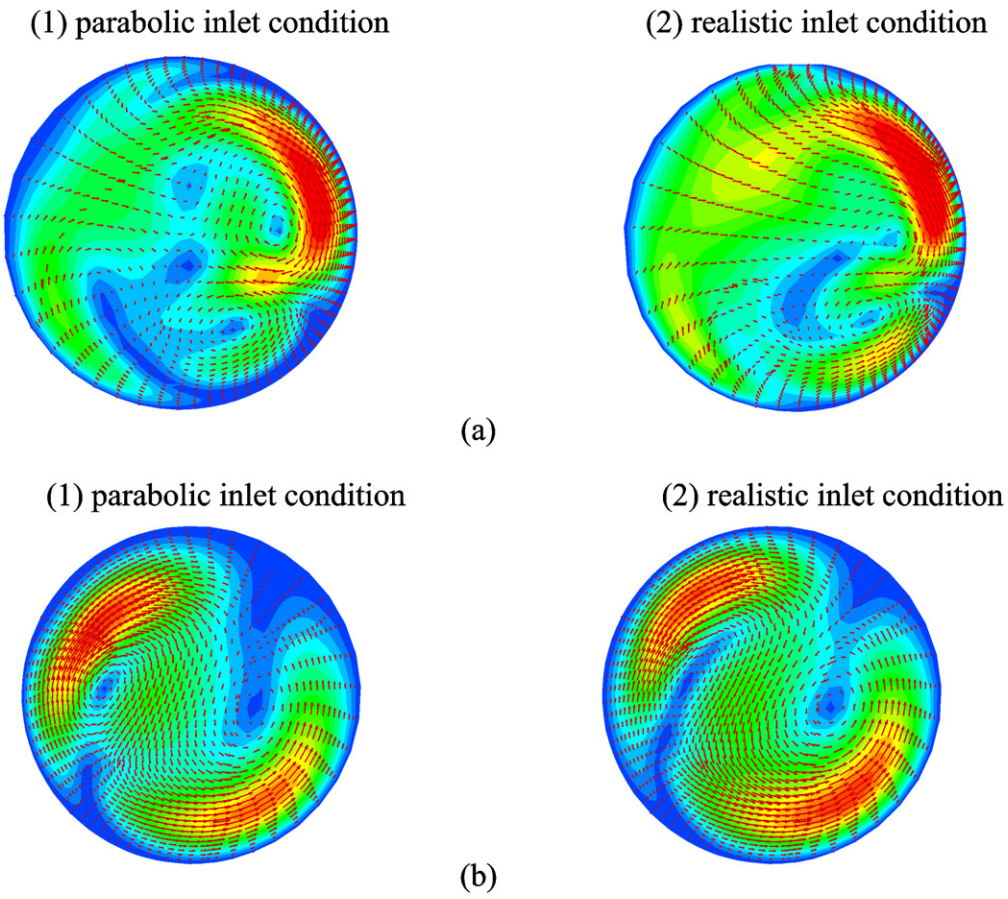

Fig. 10. Secondary flow speed and vector pattern distribution at Slice B–B′ and D–D′ ($Re_{in} = 1201$): (a1) Slice B–B′, parabolic inlet condition; (a2) Slice B–B′, realistic inlet condition; (b1) Slice D–D′, parabolic inlet condition; (b2) Slice D–D′, realistic inlet condition.

bit upwards when the realistic inlet condition was applied. The secondary flow patterns are even more similar at the two planes (see Figs. 10(a)(1), 10(a)(2), 10(b)(1) and 10(b)(2)) because the secondary flows are easier influenced by the complex geometric characteristic, i.e., spatial angles.

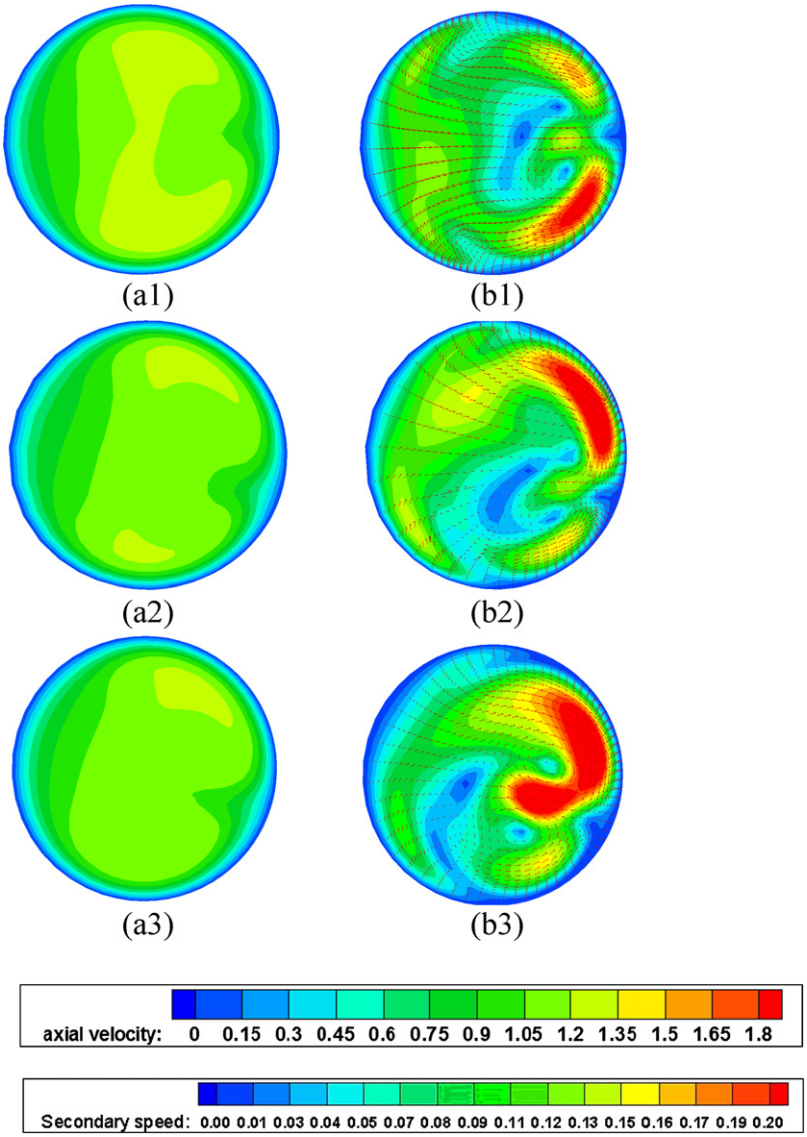

Fig. 11. Velocity distributions at Slice B–B′ with different geometric factors (realistic inlet condition, $Re_{\text{in}} = 1201$): (a1) axial velocity distribution, in-plane model; (a2) axial velocity distribution, out-of-plane model (no rings); (a3) axial velocity distribution, out-of-plane model (with rings); (b1) secondary flow speed and vector pattern distribution, in-plane model; (b2) secondary flow speed and vector pattern distribution, out-of-plane model (no rings); (b3) secondary flow speed and vector pattern distribution, out-of-plane model (with rings).

In summary, the type of inlet velocity profile may influence the airflow pattern in the airway model; however, this influence quickly diminishes for the lower lung region where the complex airway geometry plays a more important role in further flow developments.

3.3. Steady inhalation for different airway models

Geometry effects, including the spatial angle and tracheal rings, were considered by using three different airway models. In this section, flow patterns in two representative planes, i.e., Slices B–B′ and D–D′, which are located in the second and third generation, are discussed assuming the realistic inlet velocity profile ($Re_{\text{in}} = 1201$).

For the axial velocity pattern at Slice B–B′, which is located at the second order generation, it is observed that the larger velocity area in the center region (see Fig. 11(a1)) disappears in the out-of-plane model (see Fig. 11(a2)) due

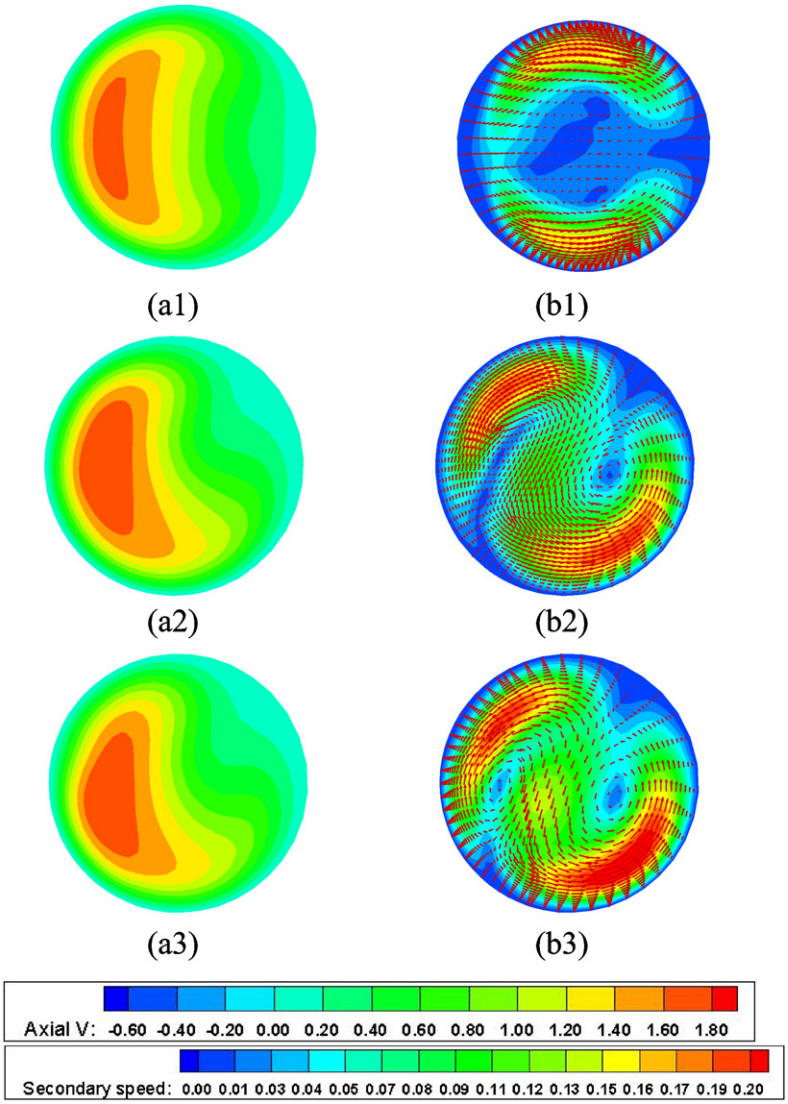

Fig. 12. Velocity distributions at Slice D–D′ with different geometric factors (realistic inlet condition, $Re_{in} = 1201$): (a1) axial velocity distribution, in-plane model; (a2) axial velocity distribution, out-of-plane model (no rings); (a3) axial velocity distribution, out-of-plane model (with rings); (b1) secondary flow speed and vector pattern distribution, in-plane model; (b2) secondary flow speed and vector pattern distribution, out-of-plane model(no rings); (b3) secondary flow speed and vector pattern distribution, out-of-plane model (with rings).

to the geometry influence. The whole flow pattern rotates clockwise. When tracheal rings are considered, the flow patterns are similar but the high-velocity region in the lower part becomes a bit weaker (compare Figs. 11(a2) and 11(a3)). Fig. 11(b1) shows the secondary flow pattern at Slice B–B′, where the associated branch features a spatial angle of 15 degrees. For the in-plane case, two apparent vortical flow regions appear. The one in the lower part near the maximum speed is stronger. Considering now the out-of-plane configuration (see Fig. 11(b2)), the stronger vortex flow appears at the upper part due to the influence of the out-of-plane geometric characteristic, i.e., mainly the spatial angle. Again, the whole flow pattern rotates clockwise. When tracheal rings were added in the out-of-plane model, the secondary flow strengthens: a peak flow region appears in center area (compare Figs. 11(b2) and 11(b3)).

Fig. 12 depicts the axial velocities and secondary flow speeds and vector patterns at Slice D–D′. When compared to the in-plane case, the upstream parent tube of Slice D–D′ rotates 25 degrees and the tube where Slice D–D′ is located rotates 60 degree. It is noted that the differences in flow structures in Slice D–D′ between two airway models are less pronounced than those in Slice B–B′, especially for the axial velocity profiles. This may indicate that the continuous

rotation of airway branches may reduce the effect of spatial angles in distal tubes. However, the differences still can be observed between the in-plane and out-of-plane configurations (see Fig. 12(b1) and 12(b2)), especially for the secondary velocities. Both axial and secondary velocity profiles rotate anti-clockwise to some degree for the out-of-plane case. Clearly, the effect of spatial angle is more significant for secondary velocity patterns because the generation of secondary flow strongly depends on the geometric feature (e.g., curvature, etc.). When tracheal rings are considered, the secondary flow pattern is similar with the smooth out-of-plane model but its intensity increases a little (compare Figs. 12(b2) and 12(b3)). This kind of strength increase is weaker than it is at Slice B–B′ because Slice D–D′ is located at a relatively distant branch, i.e., far away from the trachea. The tracheal rings influence on the axial velocity is minor. Again, the difference of the axial velocity between the ring and ring-less configurations is smaller than it is at Slice B–B′.

In summary, with the variation of spatial angles of airway branches, the axial velocity profiles in subsequent tubes may rotate to some degree and the area and magnitude of high-velocity regions may change. The effect of spatial angles is more significant for secondary velocity structures, which may result in different particle distribution. The presence of tracheal rings is felt immediately downstream flow; however, the effect decays quickly downstream. Overall, the influence of tracheal rings is less important than the influence of the spatial angles.

4. Conclusions

Employing an in-house Navier–Stokes equation solver, transient laminar inhalation with a realistic inlet waveform was simulated in an asymmetric out-of-plane human upper airway model. It is shown that the flow fields are similar to those obtained with equivalent (or matching) Reynolds numbers at steady state. However, stronger axial and secondary velocities occur at all upper branch locations during flow deceleration because of the dynamic lingering effect.

The inlet conditions, i.e., parabolic vs. realistic velocity profile, may influence steady-state flow patterns in the airway model. However, this influence vanishes further downstream because geometric complexities play an important role in local airflow development.

The spatial angle impacts significantly the secondary flow, resulting in different particle distributions (see Part II). The presence of tracheal rings may influence locally the flow pattern; however, the effect decays quickly.

Acknowledgements

This work is sponsored by the Air Force Office of Scientific Research, Air Force Material Command, USAF, under grant number FA9550-04-1-0422 (Dr. Walt Kozumbo, Program Manager).

The authors also thank Professor J.R. Edwards and Dr. X. Xiao, MAE Department, NCSU, for their assistance in adapting the finite-volume code “CFPD” for the solution of the present fluid-particle dynamics problem.

References

[1] E.R. Weibel, Morphometry of the Human Lung, Academic, New York, 1963.
[2] K. Horsfield, G. Dart, D.E. Olson, Models of the human bronchial tree, J. Appl. Physiol. 21 (2) (1971) 207.
[3] S. Ley, D. Mayer, B.S. Brook, E.J.R. Van Beek, C.P. Heussel, D. Rinck, R. Hose, K. Markstaller, H.-U. Kauczor, Radiological imaging as the basis for a simulation software of ventilation in the tracheo-bronchial tree, Eur. Radiol. 12 (2002) 2218.
[4] M.H. Tawhai, P. Hunter, J. Tschirren, J. Reinhardt, G. McLennan, E.A. Hoffman, CT-based geometry analysis and finite element models of the human and ovine bronchial tree, J. Appl. Physiol. 97 (2004) 2310.
[5] J.R. Cebral, R.M. Summer, Tracheal and central bronchial aerodynamics using virtual bronchoscopy and computational fluid dynamics, IEEE Trans. Medical Imaging 23 (8) (2004) 1021.
[6] O.G. Raabe, H.C. Yeh, G.M. Schum, R.F. Phalen, Tracheobronchial geometry, i.e. human, dog, rat, hamster LF-53, Lovelace Foundation for medical Education and Research, Albuquerque, NM, 1976.
[7] J.K. Comer, C. Kleinstreuer, Z. Zhang, Flow structures and particle deposition patterns in double-bifurcation airway models. Part 1. Air flow fields, J. Fluid Mech. 435 (2001) 25.
[8] Z. Zhang, C. Kleinstreuer, Transient airflow structures and particle transport in a sequentially branching lung airway model, Phys. Fluids 14 (2) (2002) 862.
[9] Z. Zhang, C. Kleinstreuer, C.S. Kim, Aerosol deposition efficiencies and upstream release positions for different inhalation modes in an upper bronchial airway model, Aerosol Sci. Technol. 36 (2002) 135.
[10] Z. Zhang, C. Kleinstreuer, Airflow structures and nano-particle deposition in a human upper airway model, J. Comput. Phys. 198 (2004) 178.

[11] Z. Zhang, C. Kleinstreuer, J.F. Donohue, C.S. Kim, Comparison of micro- and nano-size particle depositions in a human upper airway model, Aerosol Sci. 36 (2005) 211.
[12] N. Nowak, P.P. Kakade, A.V. Annapragada, Computational fluid dynamics simulation of airflow and aerosol deposition in human lungs, Ann. Biomedical Engrg. 31 (2003) 374.
[13] Y. Liu, R.M.C. So, C.H. Zhang, Modeling the bifurcating flow in an asymmetric human lung airway, J. Biomech. 36 (2003) 951.
[14] R.K. Calay, J. Kurujareon, A.E. Holdo, Numerical simulation of respiratory flow patterns within human lung, Respiratory Physiology and Neurobiology 130 (2002) 201.
[15] C.V. Ertbruggen, C. Hirsch, M. Paiva, Anatomically based three-dimensional model of airways to simulate flow and particle transport using computational fluid dynamics, J. Appl. Physiol. 98 (2005) 970.
[16] Y. Zhao, B.B. Lieber, Steady inspiratory flow in a model symmetric bifurcation, Trans. ASME, J. Biomech. Engrg. 116 (1994) 488.
[17] B.B. Lieber, Y. Zhao, Oscillatory flow in a symmetric bifurcation airway model, Ann. Biomedical Engrg. 26 (5) (1998) 821.
[18] G. Tanaka, T. Ogata, K. Oka, K. Tanishita, Spatial and temporal variation of secondary flow during oscillatory flow in model human central airways, J. Biomech. Engrg. 121 (1999) 565.
[19] Y. Zhang, W.H. Finlay, Measurement of the effect of cartilaginous rings on Particle Deposition in a Proximal Lung Bifurcation Model, Aerosol Sci. Technol. 39 (2005) 394.
[20] P.W. Scherer, F.R. Haselton, Convective exchange in oscillatory flow through bronchial-tree models, J. Appl. Physiol. 53 (1982) 1023.
[21] S. Mochizuki, Convective mass transport during ventilation in a model of branched airways of human lungs, in: Proceedings of PSFVIP-4, Chamonix, France, 2003.
[22] C.S. Kim, S.C. Hu, P. Dewitt, T.R. Gerrity, Assessment of regional deposition of inhaled particles in human lungs by serial bolus delivery method, J. Appl. Physiol. 81 (1996) 2203.
[23] J.R. Edwards, A low-diffusion flux-splitting scheme for Navier–Stokes calculations, Computers & Fluids 26 (6) (1997) 635.
[24] J.R. Edwards, M.-S. Liou, Low-diffusion flux-splitting methods for flows at all speeds, AIAA J. 36 (9) (1998) 1610.
[25] J.-I. Choi, R.C. Oberoi, J.R. Edwards, J.A. Rosati, An immersed boundary method for complex incompressible flows, J. Comput. Phys., in press (available online).
[26] A. Chorin, A numerical method for solving incompressible viscous flow problem, J. Comput. Phys. 2 (1967) 12.